https://dx.doi.org/10.1016/j.memsci.2020.118847

Synthesis-Structure-Performance Relationships of Nanocomposite Polymeric Ultrafiltration Membranes: A Comparative Study of Two Carbon Nanofillers

Zhishang Wan,[1,2] Yi Jiang[1,2*]

[1]Department of Civil and Environmental Engineering, The Hong Kong Polytechnic University, Kowloon, Hong Kong, China

[2]The Hong Kong Polytechnic University Shenzhen Research Institute, Shenzhen, Guangdong 518057, China

Re-Submitted to

Journal of Membrane Science

September, 2020

*To whom correspondence should be addressed:

Yi Jiang: Tel: +852-27666044; Fax: +852-23346389; Email: yi-cee.jiang@polyu.edu.hk

Abstract

Many nanoscale fillers have been impregnated in polymeric ultrafiltration membranes in order to augment performance, but their effects on membrane formation, structure, and performance remain fragmentally and poorly understood. In this work, we comparatively studied the effects of two carbon nanofillers (i.e., graphene oxide (GO) and carboxylic-functionalized carbon nanotube (c-CNT)) and established a coherent understanding of the synthesis-structure-performance relationships of such nanofiller-impregnated ultrafiltration membranes. Our results show that the morphological factor, as a result of nanoparticle properties, in addition to thermodynamic instability and rheological hindrance, is an important factor to consider when evaluating the effects of (carbon) nanofiller on membrane formation. Further, we addressed the discrepancy previously observed in rejection performance change after nanofiller addition, and demonstrated that the main benefits of adding carbon nanofillers exist in the enhancement of rejection of negatively charged molecules with increased permeability at low nanofiller mass loading. Our research findings bridge critical knowledge gaps, and provide mechanistic insights into the role and application of nanofillers in membranes.

1. Introduction

Ultrafiltration (UF) retains colloids or molecules in a dispersed media (e.g., water) through a filter with pores or interstices of similar dimensions (usually 1 to 100 nm) [1]. UF membranes are usually made by the so-called phase inversion method, during which a polymer is transformed from liquid dispersion (i.e., casting solution) to solid film [2]. Incorporation of additives (in casting solution initially) is an easily operated method with commercial promise to enhance membrane performance [3]. Among all the additives (e.g., surfactants, polymer, salt, etc.), polymers especially poly(vinyl pyrrolidone) (PVP) and poly(ethylene glycol) (PEG)) are commonly used, and their effects on thermodynamic and kinetic parameters of the phase inversion process have been well documented [4-6].

In the past decade or so, many nanoscale fillers with unique material properties were impregnated to fabricate so-called mixed-matrix membranes (MMMs), which were firstly demonstrated as gas separation membranes [7]. Recently, a large variety of nanofillers have also been applied to UF membranes, including carbon nanomaterials (e.g., C_{60} [8], carbon nanotube (CNT) [9], graphene (oxide) [10]), metals (oxides) (e.g., Ag [11], TiO_2 [12]), metal-organic frameworks (MOFs) [13], and hybrid materials [14]. Among all, carbon nanofillers including graphene oxide (GO) and carbon nanotube (CNT), have attracted great research attention due to their highly tunable structure and easiness to mass production [9, 15-17]. Such carbon allotropes have different configurations of hexagonal lattice of carbon atoms (e.g., 2D sheet for GO and 1D tube for CNT), various surface

chemistries and can form hybrids. Their size and surface chemistry can be tuned to vary by orders of magnitude [15, 18].

Nevertheless, the mechanistic understanding of nanofiller effects, in particular on membrane formation, remains incomplete. It is widely accepted that thermodynamic and rheological properties of the casting solution have large influence on membrane formation, and thus structure/performance. Current understanding was largely based on previous findings of polymeric additives-similar as polymeric additives, the presence of (hydrophilic) nanofillers was believed to change hydrophilicity and viscosity of the casting solution, which in turn results in different membrane structure [4-6]. At low mass loading, increased hydrophilicity leads to faster exchange of solvent and non-solvent, resulting in more porous membrane structure and higher surface hydrophilicity. However, with further addition of nanomaterials, the viscosity increase of the casting solution outweighs, and porosity begins to decrease, so does the permeability. Such presumptive understanding of nanofiller effects on membrane formation did not reflect the size, structural, and chemical difference of nanomaterials compared to polymeric additives. As a result, whether similar theory applies (or to which extent) needs concrete evidence.

Further, as discussed in one of our earlier reports [19], a survey of the published literature showed that the impregnation of carbon nanomaterials resulted in varied membrane permeability and selectivity, which depend on properties of the applied carbon nanomaterials (shape, surface functional groups, hybrids), mass loading, and tested solute

84 (e.g., size and charge) (See S.I. Fig. S1). The overall trend for the change of permeability
85 is that it firstly increases, then decreases with addition of (hydrophilic) nanomaterials [10,
86 19]. A peak permeability, up to ca. 41 times [20] and 13 times [21] that of control
87 membranes, was observed for GO- and CNT-modified membranes, respectively. This is
88 consistent with the change of membrane structure inferred by the role of polymer additives
89 in membrane formation (as introduced earlier). However, there has not been an overall
90 consensus on how the selectivity/rejection changes with the addition of carbon nanofillers
91 (Fig. S1). Some studies reported that the addition of GO [22-24] and CNT [25-27]
92 increased the rejection and permeability simultaneously, while others found an inverse
93 relationship between these two (e.g., GO-modified membranes [14, 28] and CNT-modified
94 membranes [9, 29, 30]). The rejection coefficient of one compound (e.g., protein BSA) in
95 these studies did not contain sufficient information to reflect the true sieving property
96 (change) of the modified membranes. Even though a few papers have studied and compared
97 the MWCO values of the nanocomposite membranes, opposite trends were reported [31,
98 32]. Overall, contrasting observations in existing literature warrant a thorough
99 investigation into the rejection mechanism(s) when nanofillers are applied.

100 In this work, we aim to establish/reveal the synthesis-structure-performance
101 relationships of nanofiller-impregnated polymeric ultrafiltration membranes by comparing
102 the effects of two commonly applied carbon nanofillers, GO and c-CNT. Specifically, we
103 address the two overlooked topics as outlined earlier: (1) how the different properties of

GO and c-CNT affect the membrane formation process during phase inversion; and (2) how the addition of carbon nanofillers affects the rejection mechanism(s). Our study includes synthesis of two types of nanocomposite membranes under systematically varied conditions; comprehensive characterization and mathematical modelling that provide delicate membrane structural information; as well as performance evaluation using a spectrum of solutes, including both neutral (dextran of varied molecular weights) and charged ones (methyl orange (MO), methylene blue (MB), and bovine serum albumin (BSA)). Taken together, our research findings bridge a few critical knowledge gaps that are needed to build detailed synthesis-structure-performance relationships of nano-enabled polymeric ultrafiltration membranes.

2. Experimental

2.1. Materials

GO was synthesized by the modified Hummer's method [33], as done and reported in our previous studies [10, 34-36]. c-CNT (20-30 nm O.D., 5-30 μm long) was purchased from Chengdu Organic Chemicals Co., Ltd, Chinese Academy of Sciences. 1-Methyl-2pyrrolidinone (NMP), polyvinylpyrrolidone (PVP, Mw 10,000) and polysulfone (PSF, beads, average Mn ~22,000) were from Sigma Aldrich. Methyl orange (MO) and methylene blue (MB) were provided by Beijing Chemical Works and Uni-Chem, respectively. Dextran (Mw 10k, 40k, 70k, 110k, 150k, 250k and 500k; medical grade) were

purchased from Aladdin Industrial Corporation (Shanghai) and bovine serum albumin (BSA) was provided by BioFroxx (Germany).

2.2. Nanomaterial Characterization

The morphology and size of nanofillers (i.e., GO and c-CNTs) were examined by transmission electron microscopy (STEM, Jeol JEM-2100F). Fourier transform infrared spectroscopy (FTIR, PerkinElmer Spectrum Two), Raman spectroscopy (Renishaw, Micro-Raman Spectroscopy System), and X-ray photoelectron spectroscopy (XPS, PHI 5000 VersaPro III) were used to study their surface chemistry. The hydrodynamic size distribution of GO and c-CNT were measured with a ZetaSizer Nano ZS (10 mg/L in NMP solution, Malvern Instruments, Worcestershire). The size distribution of GO in 200 mg/L aqueous solution was also measured.

2.3. Membrane Preparation

A typical casting solution consists of 8.1 g of NMP, 0.1 g of PVP, 1.8 g of PSF, and a desired amount of GO/c-CNT (0-5 wt. % to the PSF mass). First, 0.1 g PVP and specified amount of GO/c-CNT (0-90 mg) were directly added into 8.1 g NMP. The solution was then sonicated for 1 h to disperse these nanoparticles, followed by the addition of 1.8 g PSF beads. The mixture was stirred (200 rpm) in dark at 60 °C for 24 h to obtain a homogenous casting solution. Afterwards, it was cooled down to room temperature to remove any air bubbles. The room temperature and humidity were 22±3 ℃ and 59±3%, respectively.

Then, 4 ml of the casting solution was extracted and spread on a clean glass plate using

a four-path casting knife (BEVS 1803/80/2, BEVS Industrial Co., Ltd.) with a denominated thickness of 150 μm. Afterwards membrane casting was performed on an automatic film coater (AT-TB-2100, Animate Co., Ltd.). The formed thin film (30 × 7 cm) was immersed immediately into a water bath to initiate phase inversion. The membrane coupons that came off the glass plate was stored in deionized water before any characterization or performance evaluation.

2.4. Characterization of Membrane Formation

To characterize the rheological properties of the casting solution, viscosity (mPa•s) was measured using a dynamic shear rheometer (DSR Smart Pave 92, Anton Paar) at 22 °C. Each viscosity curve consists of 30 data points measured at 30 s interval under 1 s^{-1} shear rate. Cloud points of the casting solutions were measured to characterize their thermodynamic changes. Deionized water as the titration solution was added to the stirring casting solution until visual cloudy feature was achieved. Composition of the mixed solution (i.e., NMP, PSF, PVP, and deionized water) at the cloud point was calculated by weight [37]. Coagulation time is the period of time between immersing the wet film into water bath and its complete precipitation (i.e., the edge of the solidified membrane begins to come off the glass plate). It includes the time of diffusion of solvent and nonsolvent across the interface between casting solution and coagulation bath, and the time of precipitation of the polymer [6]. It was measured by using a stopwatch for three times (coupons) for each type of membrane.

2.5. Membrane Characterization

The surface and cross-section morphology of as-synthesized membranes was examined with a field emission scanning electron microscope (FESEM, Tescan MAIA3). The membrane cross-sections were prepared by fracturing membrane coupons in liquid nitrogen. All the samples were sputtered with gold for 90 s (BAL-TEC, SCD 005) before the FESEM examination. Water contact angles were measured via a sessile drop method. Membrane coupons were dried overnight at room temperature, and five measurements were conducted for each membrane coupon/case to obtain an average value. Membrane surface streaming potential was measured by an electrokinetic analyzer (SurPASS, Anton Paar, Graz, Austria) with an adjustable gap cell (set at 100 μm), using 1 mM KCl aqueous solution as the background electrolyte [38]. The pH of the electrolyte solution was adjusted with 5 mM HNO_3/NaOH.

Membrane overall porosity was estimated by the gravimetric method [22]. Membrane coupons were dried at room temperature for 24 h and then weighed on an electronic balance to get the dry weight (m_{dry}). The coupons were then immersed in deionized water for 24 h and the wet weight (m_{wet}) was obtained after carefully mopping the surface water with a clean tissue paper. Average membrane thickness was calculated after measuring ten points for each membrane coupon by a micrometer (Mitutoyo 293-340-30). The porosity was calculated as:

$$\varepsilon = \frac{(m_{wet} - m_{dry})/\rho_w}{S \times d_m} \quad (1)$$

where S is the surface area (19.6 cm^2) of the cut membrane, d_m is the thickness of the cut membrane, and ρ_w is density of water.

The mean pore size and pore size distribution of as-synthesized membranes were studied using a capillary flow porometer (POROLUX 1000, Germany). For each case, four coupons were measured.

2.6. Membrane Performance Evaluation

Membrane filtration performance was evaluated using a stirred cell (Sterlitech, HP4750) under a constant pressure dead-end filtration mode. Firstly, as-synthesized membranes were compacted in water under 3 bar for 30 min before measuring the pure water flux. The filtration tests were conducted at least in triplicate using 0.2 g/L dextran, 10 mg/L MO, 10 mg/L MB, and 1 g/L BSA solutions. All the solutions were stored at 4 °C and used within 2 days of preparation. The pH of the BSA solution was adjusted to 6.8-7 with 0.1 M HCl or NaOH. Membranes were soaked in BSA solutions for at least 12 h to obtain the adsorption equilibrium before BSA tests [39]. During filtration, the solution was pressurized by a nitrogen gas tank at 2 bar and stirred at 300 rpm. An electronic balance (Ohaus, SPX2201) was used to automatically log the data at a 60 s interval.

For rejection tests, filtrate fluxes were recorded for a certain period of filtration time (i.e., 30 min), followed by collecting 5 mL each of permeate and bulk solution in the stirred cell. The collected dextran solutions were measured with a TOC analyzer (TOC-L, Shimadzu, Japan) after proper dilution; and the collected MO, MB, and BSA solutions were

measured using a UV-Vis spectrophotometer (mrc Spectro UV-11) at an absorption peak of 464, 664, and 278 nm, respectively. All the tests were conducted at ambient temperature. The observed solute rejection coefficient (rejection rate) is defined as:

$$R_0 = 1 - \frac{C_p}{C_b} \quad (2)$$

where C_p is the permeate concentration and C_b is the concentration of the bulk solution.

3. Theoretical Modelling

A mathematical model developed by Ren et al. [40] was used to predict the pore size distribution of the membranes, which was shown to have fitted well the dextran rejection curves of hollow fiber membranes [40]. In essence, the model was built based on the following assumptions: a log-normal pore size distribution, Poiseuille flow in the membrane, and steric interaction between solute molecules and pores [40]. Details about the model are included in S.I..

4. Results and Discussion

4.1. Nanomaterial Characterization

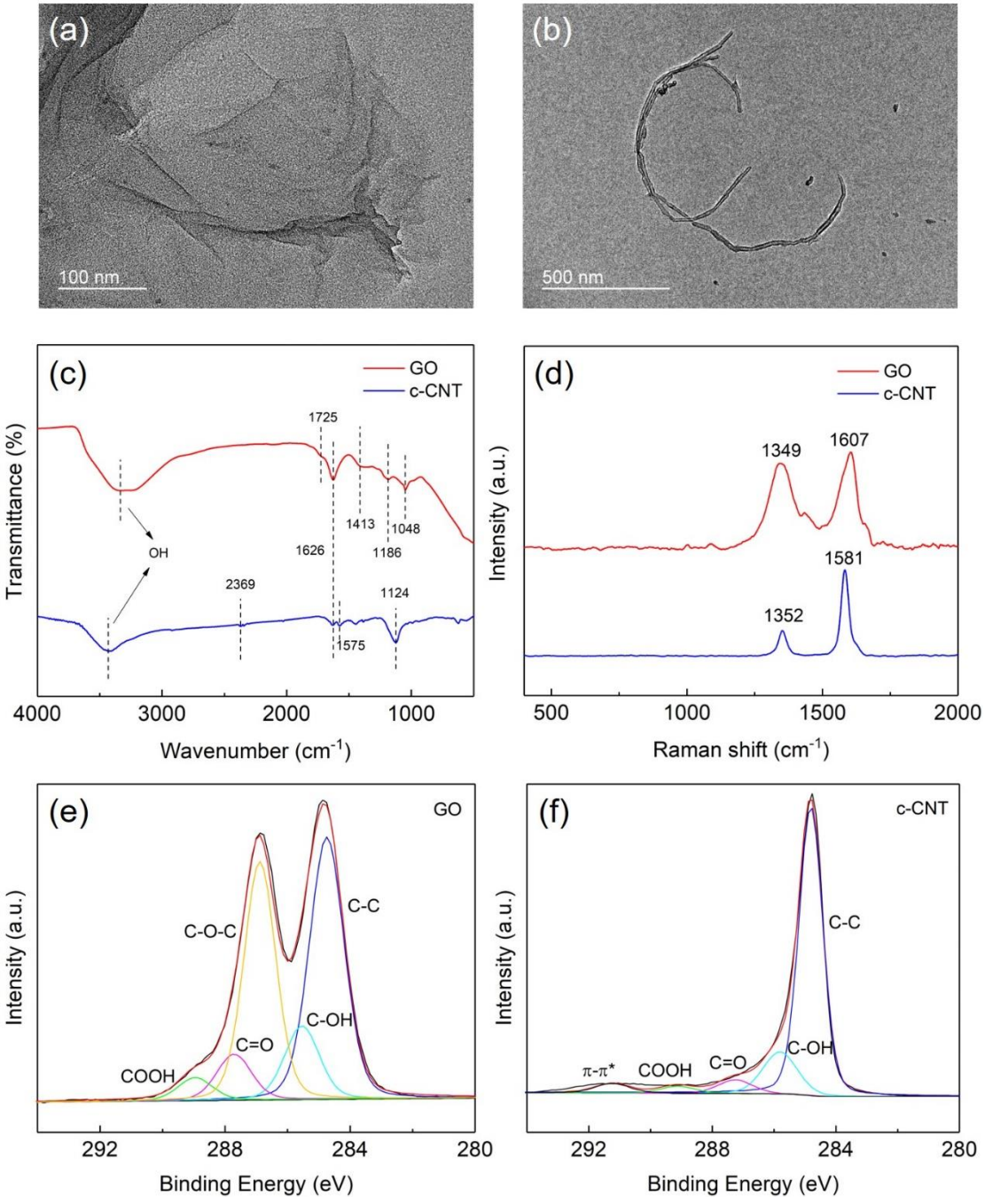

Fig. 1. TEM images of (a) GO and (b) c-CNT; (c) FTIR and (d) Raman spectra of GO/c-CNT; High resolution C1s XPS spectra of (e) GO, and (f) c-CNT. The peak positions were constrained within 0.2 eV from the assigned position, and the FWHM values were fixed at 1.1 ± 0.2 eV for all major peaks.

TEM images of GO and c-CNT are shown in Fig. 1(a) and (b), respectively. 2D GO shows a sheet-like morphology, with wrinkles at the edges, which is typically observed [36]. The single GO sheet has a lateral size of ca. 420 nm measured from the TEM image (the longest horizontal dimension), while DLS measurement shows an average hydrodynamic size of ca. 290 nm (Fig. S2(a)). This is because flat GO is treated as a sphere that has the same average translational diffusion coefficient during the DLS measurement [36]. c-CNT has a distinctive tubular structure with ca. 20 walls (Fig. 1(b) and S2(b)). The outer diameters of these tubes are measured to range from 17.5 to 21.4 nm (Fig. S2(c)), which is consistent with the values reported by the manufacturer (20-30 nm). The c-CNTs have an average length of 1.7 μm measured from TEM images (nominal length of 5-30 μm as provided by the manufacturer), probably due to fragmentation as a result of sonication.

Fig. 1(c) shows the FTIR spectra of GO and c-CNT. As described in our previous work and others [34, 36, 41, 42], oxygen-based functionalities are identified for GO, including C-O (1048 cm^{-1} from alkoxy or epoxy, 1186 and 1413 cm^{-1} from carboxyl) and C=O (1725 cm^{-1}). These oxygen containing functionalities result from the partial oxidation of graphite when synthesizing GO [42]. Further, the broad and strong peaks at ca. 3400 cm^{-1} and 1620 cm^{-1} are indicative of bound water molecules [41]. These peaks of c-CNT are weaker than those of GO, revealing higher hygroscopicity of GO (hydrophilicity). For c-CNT, a notable peak appears at 2369 cm^{-1}, which corresponds to O-H stretch from -COOH [43]. In addition, the peaks at 1575 and 1124 cm^{-1} are likely associated with the aromatic C=C bond [21, 43].

The FTIR analysis indicates that c-CNT is less oxidized than GO.

The observation from Raman spectra is consistent with that from FTIR (Fig. 1(d)). Both GO and c-CNT have two characteristic peaks, i.e., the D peak at ca. 1350 cm^{-1} and G peak at ca. 1585 cm^{-1}. The D peak can be assigned to the disordered graphite structure or sp^3-hybridized carbon [44], while the G peak is related to the splitting of the E_{2g} stretching mode of graphite, resulting from the opposite moving directions of two neighboring carbon atoms [45]. The ratio of the G peak intensity (I_G) to D peak intensity (I_D) represents the structural regularity degree of carbon nanomaterials [46]. The lower I_G/I_D value (1.1) of GO, compared with 3.5 of c-CNT, indicates that GO is more structurally defective (from harsh oxidation of graphite) than c-CNT.

Surface chemistry of GO and c-CNT is quantified by XPS as shown in Fig. 1(e) and (f), respectively. The high-resolution carbon 1s peak is deconvoluted into five oxidation states, including the C-C (284.8 eV), C-OH (~285.6 eV), C-O-C (~287.4 eV), C=O (~287.7 eV) and COOH (~288.9 eV) functionalities [10, 47]. As shown in Fig. 1(e), GO has abundant oxygen-based functional groups, including C-OH (~12% of area ratio), C-O-C (~37%), C=O (~7%), and COOH (~4%). For c-CNT, the C=O (~4%), and COOH (~2%) area ratios are lower than those of GO (~7% C=O, and ~4% COOH); the C-C (~80%) area ratio is ca. two times than that (~41 %) of GO, and the C-OH (~11%) accounts for the same ratio. Besides, the c-CNT spectrum has a π-π* (~291.2 eV) shakeup feature [48, 49].

4.2. Characterization of Membrane Formation Process

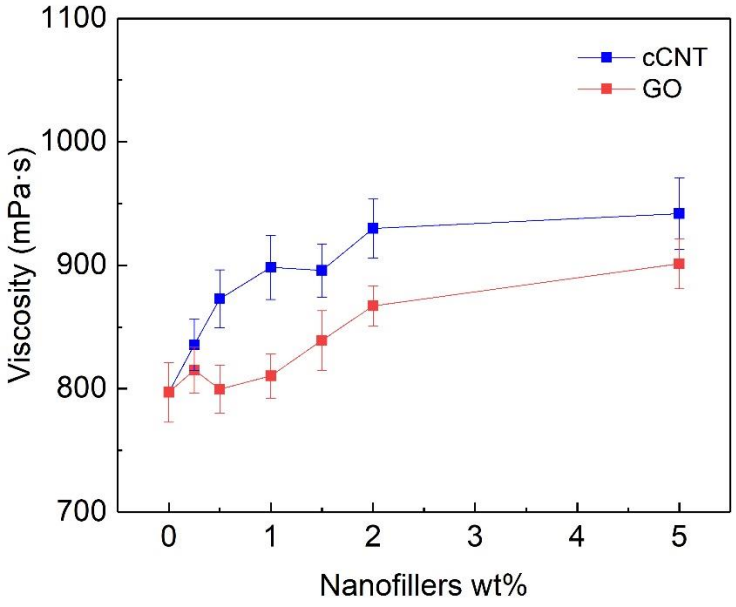

Fig. 2. Viscosity of the casting solution with 0-5 wt.% loadings of GO or c-CNT.

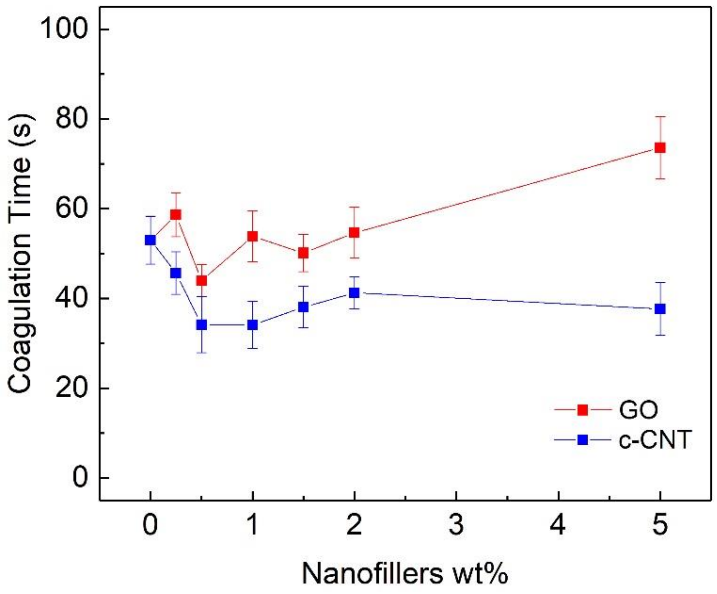

Fig. 3. Coagulation time of membrane formation with 0-5 wt.% loadings of GO or c-CNT.

277 The viscosity of a nanofluid represents its resistance to deformation at certain
278 condition, which can be affected by nanoparticle properties such as size, shape, aggregation
279 state, and concentration [50]. As shown in Fig. 2, the viscosity of the casting solution
280 increases from 797 mPa•s (without nanofiller) to 901 mPa•s and 941 mPa•s with 5.0% GO
281 and c-CNT addition, respectively. Overall, the more the added GO/c-CNT, the higher the
282 viscosity; moreover, the viscosity increases faster when c-CNT is added compared to GO
283 at low loading (< 1%); and the viscosity of c-CNT-PSF casting solution is always higher
284 than that of GO ones. It was reported that large surface area, elongated shape, and/or
285 aggregation of nanoparticles contribute to high(er) viscosity of a nanofluid [50-52]. Herein,
286 c-CNT has an elongated shape (as shown in TEM images) and more aggregation in NMP
287 solution (size measurement by DLS, Fig. S4) [53], which contribute to the higher viscosity
288 of the c-CNT-PSF casting solutions with respect to GO ones. Viscosity represents the
289 rheological factor in membrane formation, and high viscosity delays the diffusion between
290 solvent and non-solvent [5]. Our data reveals that from a rheological perspective, the
291 overall diffusion is expected to be inhibited with the addition of GO or c-CNT because of
292 increased viscosity of the casting solution, resulting in decelerated phase inversion. Also,
293 due to higher viscosity, the coagulation process of c-CNT-PSF membranes is likely slower
294 than that of GO-PSF membranes. Similar trend was observed in the case of polymeric
295 additives, including polyvinylpyrrolidone (PVP) [5] and polyether glycol (PEG) [6].

296 The cloud points of the casting solutions were measured to characterize

297 thermodynamic change(s), which represent an approximate point when liquid-liquid
298 demixing occurs [5, 6]. The casting solution prepared without GO or c-CNT becomes
299 cloudy with 4.4 wt.% water addition, which lies in the range of 1.6-6.1 wt.% as shown in
300 previous reports [5, 6]. For GO- and c-CNT-PSF casting solutions, however, it turned out
301 difficult to distinguish the solvent separation due to color interference (photos in Fig. S3).
302 Previous studies reported that the introduction of hydrophilic polymer additives (e.g., PEG
303 and PVP) can reduce the miscibility of solution with non-solvent (i.e., water), and the
304 miscibility is further decreased with incremental addition of PEG/PVP [5, 6]. This leads to
305 enhanced thermodynamic instability and accelerates phase inversion. Similarly, due to the
306 hydrophilic functional groups of GO and c-CNT, we speculate that the addition of GO or
307 c-CNT works in favor of enhancement in the demixing of the solutions thermodynamically,
308 and the addition of GO likely induces faster demixing with respect to that of c-CNT because
309 of its higher hydrophilicity.

310 Previous studies mainly concluded that membrane formation/structure is determined
311 by rheology and thermodynamics of the casting solution [10, 54, 55]. If so, their combined
312 effects could be reflected in coagulation time of the membrane formation (Fig. 3). At low
313 mass loading (i.e., < 0.5%), the coagulation time decreases from 53.0 s (without nanofillers)
314 to 43.9 s and 34.2 s for 0.5% GO- and c-CNT-PSF membrane, respectively. Then the
315 coagulation time increases to 54.7 s and 41.3 s for 2.0% GO- and c-CNT-PSF membrane,
316 respectively. However, it continues to increase for GO-PSF membrane (73.6 s for 5.0%

GO-PSF membrane), but decreases to 37.7 s for 5.0% c-CNT-PSF membrane. In the low mass loading range, the overall trend of change is consistent with previous literature that enhanced hydrophilicity increases thermodynamic instability (which outweighs the increase of viscosity) and thus leads to faster exchange of solvent and non-solvent [10, 53, 56]; and with further addition of nanomaterials, the viscosity increase of the casting solution outweighs, which delays demixing, and thus the coagulation time increases [10].

Interestingly, the coagulation time of c-CNT-PSF membrane formation is always shorter than that of GO-PSF membrane, and the difference becomes more significant when more GO/c-CNT are added. This observation regarding c-CNT-PSF membrane contrasts with the earlier hypothesis that rheology and thermodynamics together determine the coagulation process, because both rheological and thermodynamic changes in case of adding c-CNT disfavor faster coagulation compared to GO. We attribute this deviation to a morphological factor related to the properties of c-CNT (i.e., the hollow structure and the aggregation/dispersion state in organic solvent), which likely creates (more) porous/defective surface/skin layer and accelerates the exchange between solvent and non-solvent, and finally the coagulation process. As shown before, such change of surface morphologies of the nascent skin layer directly influenced formation kinetics of membrane via phase inversion, where more/larger surface pores were shown to accelerate the separation [6]. Initially, a more porous/open surface structure facilitates the exchange of solvent and non-solvent, also leading to thinner skin. As revealed in the DLS measurement

(Fig. S4), c-CNT has a poorer dispersibility compared to GO in NMP, which potentially results in aggregates/non-uniform distribution in the surface. In another word, the combined effects of thermodynamic instability and rheological hindrance largely affect the formation of GO-PSF membranes, as previous studies have identified [10, 57]; while an additional factor (i.e., the morphological factor related to c-CNT) comes into play and accelerates the formation of c-CNT-PSF membranes. More evidence can be found in the S.I. (Fig. S5). This morphological factor will become apparent for some nanoscale fillers, as a result of their properties, especially aggregation/dispersion state in organic solvent. Detailed membrane characterization results support the role of an additional morphological factor which are discussed later.

4.3. Membrane Characterization

Table 1 Estimated membrane total thickness, porosity; and water contact angle (WCA) of 0%, 0.5%, 2.0%, and 5.0% GO- and c-CNT-PSF membranes.

Membranes	Total Thickness (μm)	Porosity	WCA (°)
PSF	74.9 ± 2.9	0.77 ± 0.06	77.1 ± 3.5
0.5% GO	70.9 ± 3.4	0.78 ± 0.03	73.4 ± 3.6
2.0% GO	70.9 ± 1.2	0.79 ± 0.01	61.7 ± 4.6
5.0% GO	73.1 ± 0.8	0.78 ± 0.01	61.6 ± 5.7
0.5% c-CNT	71.2 ± 4.1	0.81 ± 0.05	72.4 ± 4.1

2.0% c-CNT	71.2 ± 1.4	0.81 ± 0.02	62.4 ± 3.2
5.0% c-CNT	71.7 ± 1.2	0.79 ± 0.02	55.8 ± 3.1

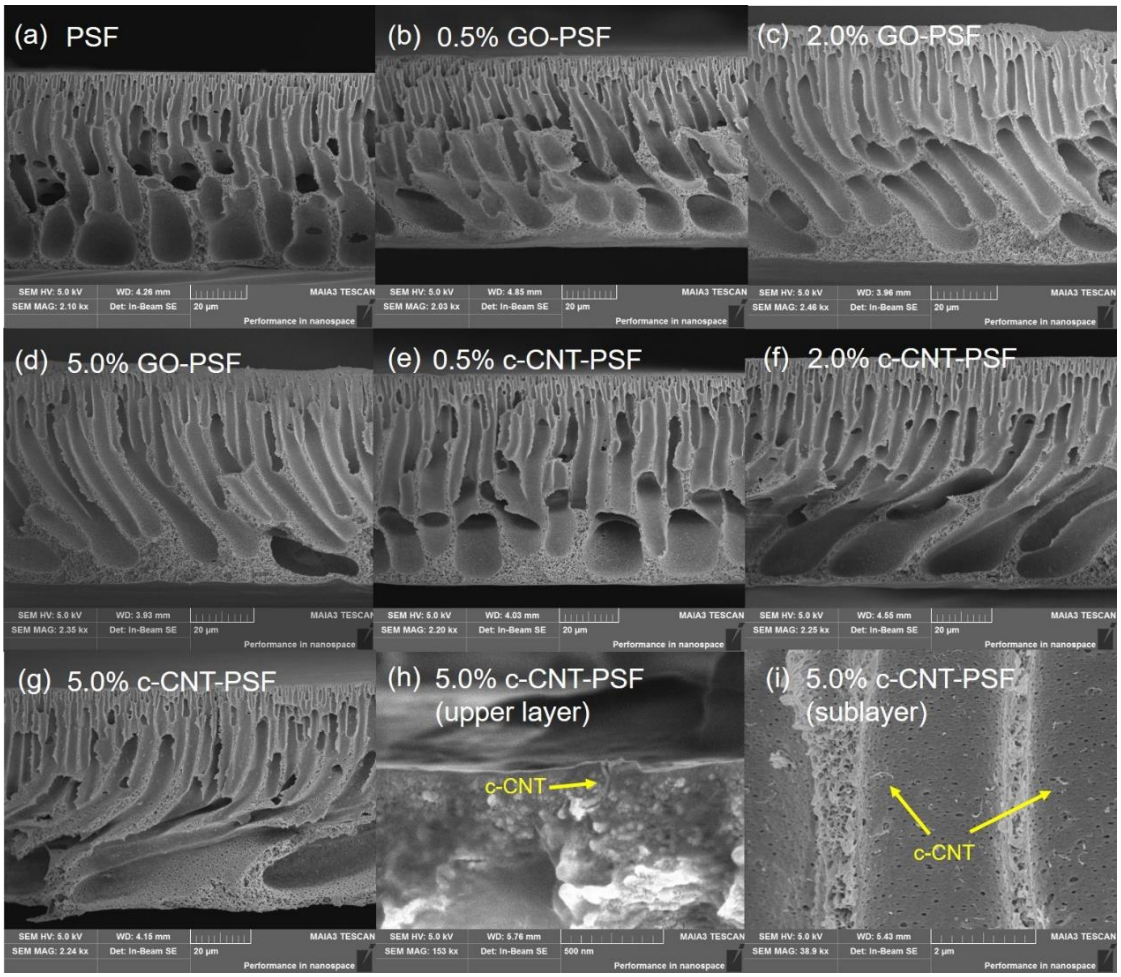

Fig. 4. FESEM images of the cross-sections of PSF membranes impregnated with different amount of carbon nanofillers: (a) 0%, (b) 0.5% GO, (c) 2.0% GO, (d) 5.0% GO, (e) 0.5% c-CNT, (f) 2.0% c-CNT, and (g) 5.0% c-CNT; (h) the upper layer and (i) the sublayer of 5.0% c-CNT-PSF membrane.

The cross-sectional FESEM images of 0%, 0.5%, 2.0%, and 5.0% GO- and c-CNT-PSF membranes are shown in Fig. 4. All membranes show a typical asymmetric structure (Fig. 4(a-g)), irrespective of the GO/c-CNT addition in the casting solution. Membranes

363 prepared with 2.0% and 5.0% c-CNT show enlarged macropores (Fig. 4(f) and 4(g),
364 respectively). A previous study also found enlarged macropores of polyacrylonitrile (PAN)
365 membranes with high CNT loading, which were attributed to fusion from other pores [30].
366 More importantly, aggregates of c-CNTs or c-CNT-PSF bumps were observed to emerge
367 from the membrane surface for 2.0% and 5.0% c-CNT-PSF membranes, however, these
368 features were not observed for GO-PSF membranes, consistent with our earlier report [10]
369 (Fig. S6). For carbon nanotubes, material observation on the surface of similar membranes
370 occurred with mass percentages as low as 1% [58]. Fig. 4(h) and 4(i) directly showed the
371 existence of c-CNT in the upper and sublayer of 5.0% c-CNT-PSF membranes (yellow
372 arrows). The existence of GO/c-CNT in the upper layer can also be supported by the color
373 change of the 5.0% GO-, and 5.0% c-CNT-PSF membranes (Fig. S7). The color difference
374 between the top- and back-view becomes obvious with 5.0% GO/c-CNT addition. Overall,
375 these structural differences support the existence and role of the morphological factor
376 related to c-CNT, which leads to fast solvent demixing and the formation of enlarged
377 macropores.

378 Table 1 lists the estimated membrane thickness, overall porosity and measured water
379 contact angle (WCA) of as-synthesized membranes. For total thickness, nanocomposite
380 membranes are slightly thinner with respect to PSF membrane (~72 μm vs. 75 μm) (Table
381 1). Measured overall porosity (0.79-0.81) of c-CNT-PSF membranes (0.5-5.0% addition)
382 are slightly larger than that (0.78-0.79) of GO-PSF membranes, while PSF membrane has

383 the lowest porosity (i.e., 0.77) (Table 1).

384 Water contact angle (WCA) is commonly used to indicate membrane surface
385 hydrophilicity. WCA reflects the pore intrusion behavior of water molecules, where
386 spontaneous wicking happens for a hydrophilic surface, and non- or slow wetting occurs
387 for a hydrophobic surface [59]. All nanocomposite membranes have lower WCA (Table 1).
388 With the addition of 2.0% GO and c-CNT, the average WCA decreases from 77.5° of
389 control to 61.7° and 62.4° respectively. The decrease is extensively observed and attributed
390 to the migration of GO/c-CNT to the membrane surface, increasing hydrophilic oxygen-
391 containing functional groups at the surface [21-23, 26, 57, 60]. GO-PSF membranes are
392 expected to be more hydrophilic than c-CNT-PSF membranes due to the larger oxidation
393 degree of GO than c-CNT (Fig. 1(c)-(f)). However, further additon (>2.0%) of nanofillers
394 does not result in lower WCA of GO-PSF membranes, likely due to high viscosity
395 preventing (further) migration of GO partciles to the surface. Instead, lower WCA is
396 obseved for c-CNT-PSF membranes, which is likely related to the surface structural
397 changes by c-CNT (aggregates) on membrane surface (Fig. S6) [21, 23, 60]. Herein, the
398 morphological factor related to c-CNT may have contributed to the lowest WCA of 5.0%
399 c-CNT-PSF membrane.
400

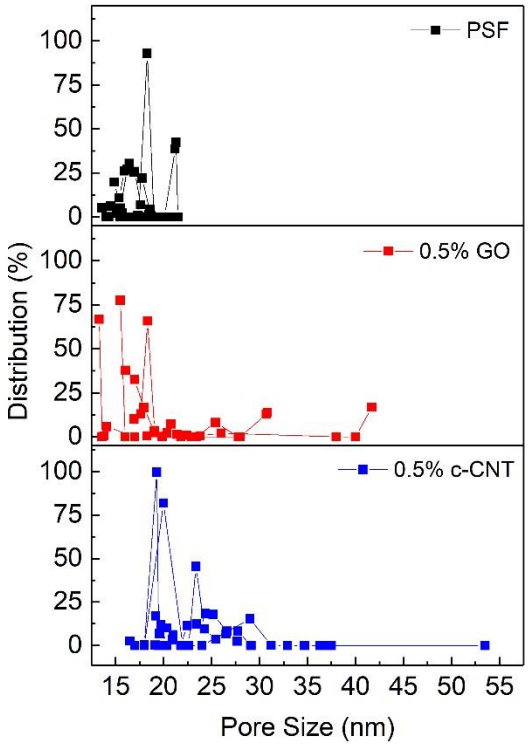

Fig. 5. The pore size distribution of PSF, 0.5% GO- and c-CNT-PSF membranes (four membranes were measured for each case).

Fig. 5 shows the pore size distribution of the PSF, 0.5% GO-PSF, and 0.5% c-CNTPSF membrane measured by a capillary flow porometer. Compared to PSF membrane with an average pore size of 18.3 ± 0.2 nm, the average pore size of the 0.5% GO- and c-CNT-PSF membrane increases to 20.5 ± 0.7 nm and 21.8 ± 0.3 nm, respectively. It is also clear that the pore size distribution widens after nanomaterial addition (Fig. 5). For PSF membrane, the pore sizes mostly span from 14 to 21 nm; for GO-PSF membrane, the pore size range expands to 15-43 nm, with the generation of some large pores (30 nm and 42 nm); and for c-CNT-PSF membrane, the range becomes 16 to 54 nm, with increased size of most large pores (18-32 nm). Pore size is the critical factor determining the sieving property of UF membranes, and this change in pore size is well reflected in the permeation and rejection performance as seen later.

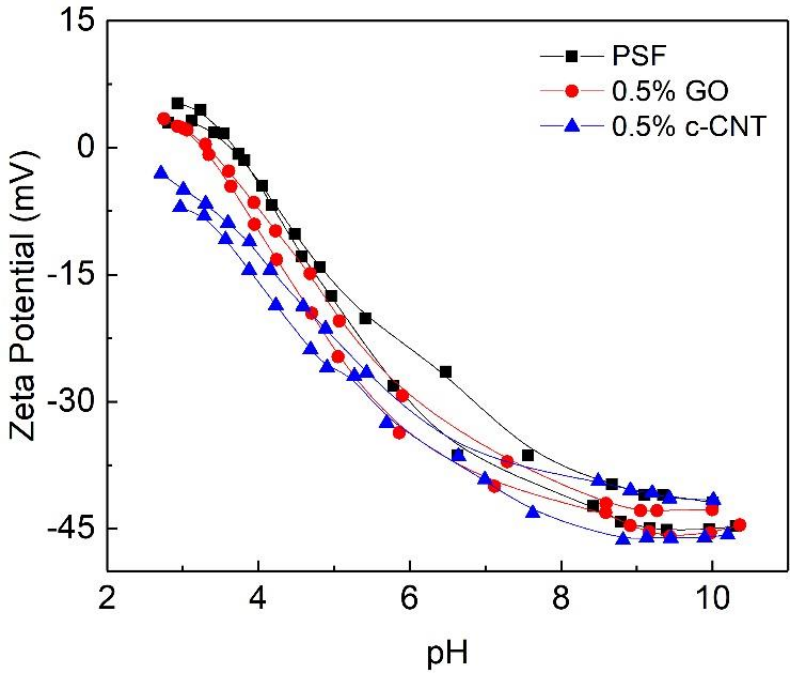

Fig. 6. Membrane surface zeta potential plotted against pH for PSF, 0.5% GO- and c-CNT-PSF membranes (two membrane coupons of each kind were tested).

The zeta potential of the membrane surfaces is measured using a streaming potential technique (Fig. 6) [61, 62]. Membrane surface acquires surface charge in aqueous solution through dissociation of surface functional groups, and/or adsorption of ions/charged molecules [61]. Overall, all membrane surfaces are negatively charged over a wide range of pH (4-10). The zeta potential increases (becomes more negative) with the increase of pH, due to more deprotonated functional groups at a higher pH [62]. When pH is near circumneutral (where our filtration experiments are conducted), the nanocomposite membranes are observed to have slightly higher (more negative) average zeta potentials with respect to controls. This is because of the dissociation of more oxygen-containing

functional groups (associated with the migrated nanofillers) at the surface, consistent with the decreasing trend of water contact angles (77° of control membrane vs. 72-73° of nanocomposite membranes, Table 1).

4.4. Membrane Performance Evaluation

4.4.1. Pure Water Permeability

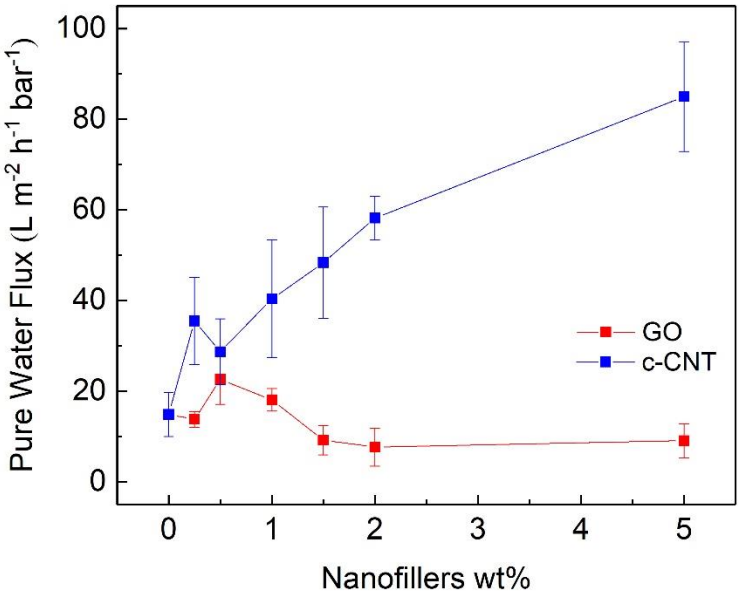

Fig. 7. Pure water flux of membranes with mass loading of 0-5% GO or c-CNT.

Fig. 7 shows the pure water flux of PSF membranes with 0-5.0% mass loading of nanofillers. Pure water flux of GO-impregnated membranes increases from 14.9 ± 4.9 LMHB (PSF control) to 22.6±5.5 LMHB (0.5% GO-PSF), and then decreases to 9.2±3.2 LMHB (1.5% GO-PSF). Further addition of GO from 1.5% to 5% just slightly decreases the pure water flux (9.1±3.7 LMHB for 5.0% GO-PSF membrane). The permeability trend (first increase and then decrease) of GO-PSF membranes is consistent with previous reports

445 [10, 14, 24, 57]. The permeability trend of c-CNT-PSF membranes is to some degree
446 different from that of GO-PSF membranes. The pure water flux increases first to 35.5±9.6
447 LMHB (0.25% c-CNT-PSF), and then it turns to a decrease (to 28.7±7.3 LMHB at 0.5%
448 addition). Afterwards it increases all the way to 85.0±12.0 LMHB (5.0% c-CNT-PSF),
449 which is ca. 6 times that of PSF membranes. From these results, three observations can be
450 made: first, the addition of GO or c-CNT leads to a peak permeability at low mass loading;
451 second, permeability of GO-PSF membranes decreases while that of c-CNT-PSF
452 membranes increases starting from 0.5% addition; finally, the permeability of c-CNT-PSF
453 membranes are all higher than those of GO-PSF membranes.

454 Generally, the observed variation of water permeability can be well supported by the
455 membrane formation kinetics and structural characters discussed in previous sections. For
456 example, further addition of c-CNT (from 0.5 to 5.0%) increases membrane permeability,
457 due to its porous structure (increased porosity and enlarged pore size), which are caused by
458 the morphological factor related to c-CNT (aggregates).

4.4.2. Filtration of Dextran Solutions

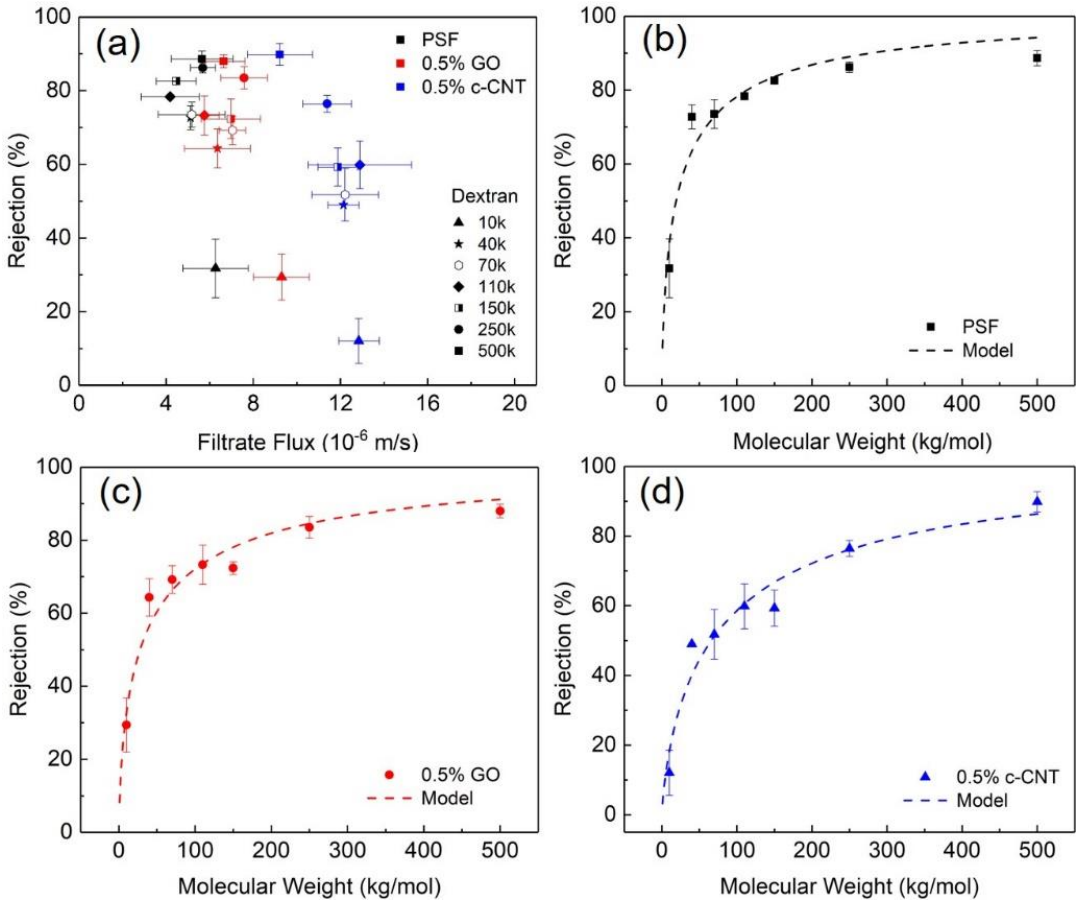

Fig. 8. (a) Rejection and filtrate flux of PSF, 0.5% GO- and c-CNT-PSF membranes using dextran as model solutes. Dextran rejection curves of (b) PSF, (c) 0.5% GO-, and (d) 0.5% c-CNT-PSF membrane.

To reveal the change(s) of sieving properties/mechanisms, we first compare the rejection of dextran by 0.5% GO- and c-CNT-PSF membranes. Dextran is a neutral slightly-branched polymer of D-glucopyranose, electrostatic properties and deformation of which are negligible during the filtration [63]. The rejection coefficients of dextran with different molecular weights and filtrate (water) fluxes are plotted in Fig. 8(a). A trade-off relationship between permeability and dextran rejection is observed. When filtering 10k

Da dextran solution, while the filtrate flux decreases from 23.1±1.7 LMHB of c-CNT-PSF membrane to 16.7±2.3 LMHB of GO-PSF membrane, and further decreases to 11.3±2.7 LMHB of PSF membrane, the rejection coefficients of c-CNT-PSF membrane increases from 12.1 ± 6.5% to 29.4 ± 6.2% and 31.8 ± 8.0 % for GO-PSF and PSF membrane, respectively. However, such trend becomes less apparent when the molecular weight of dextran increases. When the molecular weight increases to 500k Da, all the rejection coefficients reach a similar level, nearly 90%. This is because the size (27.6 nm) of 500k Da dextran is larger than the average pore size of all the membranes. This shows that the size-based (sieving) mechanism dominates [10].

Fig. 8(b-d) presents the rejection curves of dextran molecules of Mw. 10k to 500k Da by as-synthesized membranes (with 0.5% addition). It is observed that the rejection curve (rejection of different solutes plotted as a function of their molecular weight) of GO-PSF membrane rises less sharply compared to that of control membrane; while it becomes considerably smooth for c-CNT-PSF membranes (Fig. 8(b-d)). The curves are consistent with the pore size distribution measured by capillary flow porometer (Fig.5). The pore size distribution influences the steepness of the curve. Generally, the steeper the rejection curve, the smaller the mean pore size and/or the narrower the pore size distribution. The mathematical model also shows a similar trend of change related to pore size distribution (see in S.I. Fig S8 and Table S1). From model calculation, PSF membrane has the narrowest pore size distribution, and the smallest pore size (14.7 nm), while c-CNT-PSF membrane

has the widest distribution, and the largest pore size (25.7 nm). Taken together, the addition of GO or c-CNT increases the mean pore size and widens pore size distribution, which in turn decreases the sieving properties of neutral molecules such as dextran.

4.4.3. Filtration of Dye Solutions

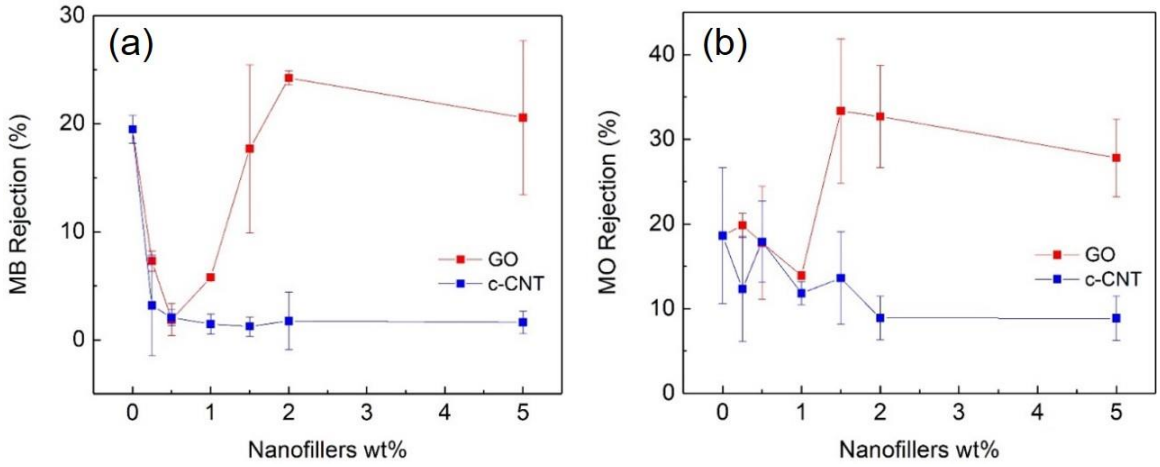

Fig. 9. (a) MB rejection and (b) MO rejection of membranes vs. loading 0-5% GO or c-CNT.

We then evaluate the rejection of small, charged molecular dyes (MO, 327 Da; MB, 284 Da) by as-synthesized membranes (Fig. 9(a) and (b)). The pH of MO and MB solutions are 7.8 and 7.4, respectively. MO molecules are negatively charged due to presence of (deprotonated) sulfonate groups [64], while MB molecules are positively charged due to existence of quaternary ammonium cations ($[NR_4]^+$) [17, 28, 65]. At low mass loadings (< 0.5%), both GO- and c-CNT-PSF membranes have similar rejection of MO or MB. With further addition of nanomaterials, the rejection by the two membranes differs markedly,

with c-CNT-PSF membrane having much lower (and nearly same) rejection. This coincides strongly with the degree of change of membrane structure/permeability. The morphological factor related to c-CNT comes into play, which results in porous structure and thus low rejection of dyes, regardless of their charges. The overall observation suggests that the size-based rejection (sieving) mechanism dominates, or the change of membrane pore size has a major impact on solute retention, which is consistent with our previous study [10].

But the charge-based mechanism also plays a role. The rejection of MO is observed to be always higher than that of MB. For example, for 0.5% GO-PSF membranes, the rejection of MO is 17.8±6.7% compared to 1.9±1.5% of MB. This can largely be attributed to the charge-based mechanism considering similar sizes of the two molecules. Also, when 0.5% GO or c-CNT is added, decreased rejection of MB and MO were observed due to enlarged membrane pore sizes (Fig. 5), but the degree of decrease in MO rejection is smaller than that of MB rejection for both membranes (for MB, rejection decreases by ca. 18%; but for MO, rejection only decreases by ca. 2%). This shows that addition of hydrophilic nanofillers provides stronger electrostatic repulsion towards negatively charged molecules (i.e., MO), which abates such decrease in rejection. It is also noteworthy that such charge-based mechanism is (comparatively) more significant in case of low water permeability (small pores), but not outstanding in case of high water permeability (such as the case of membranes with high loading of c-CNT). This implicates that the importance of the charge-based mechanism is pore size and solute-size dependent, as electrostatic

repulsion interactions will be range-dependent.

4.4.4. Filtration of BSA Solutions

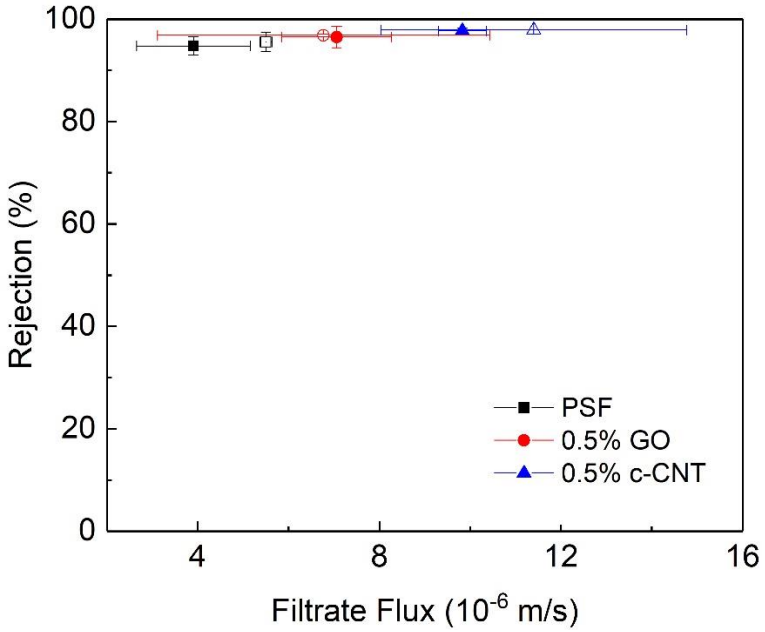

Fig. 10. Rejection and filtrate flux of PSF, 0.5% GO- and c-CNT-PSF membranes using BSA as a model solute (solid symbols: non-filtered BSA solution; hollow symbols: pre-filtered solution).

We finally evaluate the filtration of BSA solutions by as-synthesized membranes to further elucidate the size of a negatively charged molecule on rejection (Fig. 10). BSA is a negatively charged, much larger serum albumin protein compared to dyes (Mw 66.5k Da), with an isoelectric point of 4.7 at room temperature [66]. The negative charge was confirmed by a previous electrophoretic light scattering measurement (at pH ~6.9) [34]. The permeability trend is the same as filtering dextran: the filtrate flux of 0.5% c-CNT-PSF membrane (17.7±0.9 LMHB) is the highest while that of PSF membrane is the lowest (7.0 ±2.3 LMHB). However, little difference (< 5%) was observed for the rejection coefficients

(> 90%), whereas the rejection of MO is decreased after nanofiller addition. Such high rejection is consistent with a number of previous reports [10, 21, 32, 57, 60].

In Fig. 10, both non-filtered and pre-filtered (using a commercial PES membrane of 150k Da MWCO, Microdyn Nadir) BSA solutions have shown a similarly high rejection rates, which rule out the possibility of high rejection being caused by soluble aggregates via disulphide bonding in solution [67]. Further, all membranes with and without BSA pre-adsorption still have similar rejection rates (> 90%). A neutral branched molecule with similar molecular weight as BSA would have a rejection of ca. 50-70% based on the rejection curves in Fig. 8. The addition of GO or c-CNT results in enhanced surface hydrophilicity/charge, increasing the rejection of (negatively) charged molecules such as MO and BSA. Compared to MO, the (relatively) large size of BSA enables effective interactions with the pore/surface, providing sufficient electrostatic repulsion. As a result, the eventual rejection of BSA by all membranes is observed to be similarly high. This indicates that when considering the charge-based mechanism, the size of the solute is equally important which determines the effective interaction range. This might be one of the reasons that have contributed to the controversial observations of rejection change in literature. The rejection will be together decided by the interplay between membrane surface (pore size and charge) and solute properties (size, charge, etc.).

5. Conclusions

In this study, we comprehensively revealed the synthesis-structure-performance relationships of GO- and c-CNT-PSF membrane, which provides the analysis framework for additive incorporation into UF membrane via phase inversion. In particular, the relations between synthesis and structure of nanocomposite membranes were revealed, which is a new perspective compared with many previous reports focusing on the structure-performance relationships. In detail, this work highlights an additional factor, i.e., the so-called morphological factor, rooted in nanoparticle properties, to be considered in membrane formation via phase inversion. Our work also detailed the rejection mechanism(s) after nanofiller addition, which provides insights into the existing controversial observations of rejection performance change in literature. The rejection mechanism(s) will depend on the change of membrane properties (such as pore size and surface charge) and solute properties (size, charge). Adding carbon nanofillers such as GO or c-CNT at low mass loading is mainly beneficial to the rejection of negatively charged solutes (e.g., MO and BSA) with increased permeability. Nanofiller effects on other aspects of membrane performance such as antifouling and mechanical strength might be a direction of future research. Also, future work can be devoted to augment such enhancement mechanism so as to realize the full potential of nanofillers in membrane application.

Acknowledgements

This work was supported by Hong Kong Research Grants Council's Early Career Award

(25209819) and Theme-based Research Scheme (T21-711/16-R), National Natural Science Foundation of China (51908479), and Research Institute for Sustainable Urban Development, The Hong Kong Polytechnic University (1-BBWG). The authors thank Dr. Hao Guo (The University of Hong Kong) for the help with streaming potential measurement, and Prof. Bin Zhao (Tiangong University) and Prof. Hu Yanjie (East China University of Science and Technology) for the help with pore size measurement.

References

[1] J.D. Ferry, Ultrafilter Membranes and Ultrafiltration, Chemical Reviews, 18 (1936) 373-455.

[2] G.R. Guillen, Y. Pan, M. Li, E.M.V. Hoek, Preparation and Characterization of Membranes Formed by Nonsolvent Induced Phase Separation: A Review, Industrial & Engineering Chemistry Research, 50 (2011) 3798-3817.

[3] I.M. Wienk, R.M. Boom, M.A.M. Beerlage, A.M.W. Bulte, C.A. Smolders, H. Strathmann, Recent advances in the formation of phase inversion membranes made from amorphous or semi-crystalline polymers, Journal of Membrane Science, 113 (1996) 361-371.

[4] J.-H. Kim, K.-H. Lee, Effect of PEG additive on membrane formation by phase inversion, Journal of Membrane Science, 138 (1998) 153-163.

[5] M.-J. Han, S.-T. Nam, Thermodynamic and rheological variation in polysulfone solution by PVP and its effect in the preparation of phase inversion membrane, Journal of Membrane Science, 202 (2002) 55-61.

[6] Q.-Z. Zheng, P. Wang, Y.-N. Yang, Rheological and thermodynamic variation in

603 polysulfone solution by PEG introduction and its effect on kinetics of membrane formation
604 via phase-inversion process, Journal of Membrane Science, 279 (2006) 230-237.
605 [7] H.B. Park, J. Kamcev, L.M. Robeson, M. Elimelech, B.D. Freeman, Maximizing the
606 right stuff: The trade-off between membrane permeability and selectivity, Science, 356
607 (2017) eaab0530.
608 [8] J.S. Taurozzi, C.A. Crock, V.V. Tarabara, C60-polysulfone nanocomposite membranes:
609 Entropic and enthalpic determinants of C60 aggregation and its effects on membrane
610 properties, Desalination, 269 (2011) 111-119.
611 [9] J. Choi, J. Jegal, W. Kim, Fabrication and characterization of multi-walled carbon
612 nanotubes/polymer blend membranes, Journal of Membrane Science, 284 (2006) 406-415.
613 [10] Y. Jiang, Q. Zeng, P. Biswas, J.D. Fortner, Graphene oxides as nanofillers in
614 polysulfone ultrafiltration membranes: Shape matters, Journal of Membrane Science, 581
615 (2019) 453-461.
616 [11] K. Zodrow, L. Brunet, S. Mahendra, D. Li, A. Zhang, Q. Li, P.J. Alvarez, Polysulfone
617 ultrafiltration membranes impregnated with silver nanoparticles show improved biofouling
618 resistance and virus removal, Water Research, 43 (2009) 715-723.
619 [12] A. Razmjou, J. Mansouri, V. Chen, The effects of mechanical and chemical
620 modification of TiO2 nanoparticles on the surface chemistry, structure and fouling
621 performance of PES ultrafiltration membranes, Journal of Membrane Science, 378 (2011)
622 73-84.
623 [13] H. Sun, B. Tang, P. Wu, Development of hybrid ultrafiltration membranes with
624 improved water separation properties using modified superhydrophilic metal-organic
625 framework nanoparticles, American Chemical Society Applied Materials and Interfaces, 9
626 (2017) 21473-21484.
627 [14] L. Yu, Y. Zhang, B. Zhang, J. Liu, H. Zhang, C. Song, Preparation and characterization
628 of HPEI-GO/PES ultrafiltration membrane with antifouling and antibacterial properties,

629 Journal of Membrane Science, 447 (2013) 452-462.
630 [15] Y. Jiang, P. Biswas, J.D. Fortner, A review of recent developments in graphene-enabled
631 membranes for water treatment, Environmental Science: Water Research and Technology,
632 2 (2016) 915-922.
633 [16] S.C. Smith, D.F. Rodrigues, Carbon-based nanomaterials for removal of chemical and
634 biological contaminants from water: a review of mechanisms and applications, Carbon, 91
635 (2015) 122-143.
636 [17] W. Duan, A. Ronen, S. Walker, D. Jassby, Polyaniline-coated carbon nanotube
637 ultrafiltration membranes: enhanced anodic stability for in situ cleaning and electro-
638 oxidation processes, American Chemical Society Applied Materials and Interfaces, 8 (2016)
639 22574-22584.
640 [18] N. Karousis, N. Tagmatarchis, D. Tasis, Current progress on the chemical modification
641 of carbon nanotubes, Chemical Reviews, 110 (2010) 5366-5397.
642 [19] Y. Jiang, B. Peng, Z. Wan, C. Kim, W. Li, J. Fortner, Nanotechnology as a Key Enabler
643 for Effective Environmental Remediation Technologies, in: A New Paradigm for
644 Environmental Chemistry and Toxicology, Springer, 2020, pp. 197-207.
645 [20] C.A. Crock, A.R. Rogensues, W. Shan, V.V. Tarabara, Polymer nanocomposites with
646 graphene-based hierarchical fillers as materials for multifunctional water treatment
647 membranes, Water Research, 47 (2013) 3984-3996.
648 [21] W. Wang, J. Shi, J. Wang, Y. Li, N. Gao, Z. Liu, W. Lian, Preparation and
649 characterization of PEG-g-MWCNTs/PSf nano-hybrid membranes with hydrophilicity and
650 antifouling properties, Royal Society of Chemistry Advances, 5 (2015) 84746-84753.
651 [22] J. Zhang, Z. Xu, W. Mai, C. Min, B. Zhou, M. Shan, Y. Li, C. Yang, Z. Wang, X. Qian,
652 Improved hydrophilicity, permeability, antifouling and mechanical performance of PVDF
653 composite ultrafiltration membranes tailored by oxidized low-dimensional carbon
654 nanomaterials, Journal of Materials Chemistry A, 1 (2013) 3101–3111.

655 [23] Z. Xu, J. Zhang, M. Shan, Y. Li, B. Li, J. Niu, B. Zhou, X. Qian, Organosilane-
656 functionalized graphene oxide for enhanced antifouling and mechanical properties of
657 polyvinylidene fluoride ultrafiltration membranes, Journal of Membrane Science, 458
658 (2014) 1-13.
659 [24] S. Zinadini, A.A. Zinatizadeh, M. Rahimi, V. Vatanpour, H. Zangeneh, Preparation of
660 a novel antifouling mixed matrix PES membrane by embedding graphene oxide nanoplates,
661 Journal of Membrane Science, 453 (2014) 292-301.
662 [25] Y. Mansourpanah, S.S. Madaeni, A. Rahimpour, M. Adeli, M.Y. Hashemi, M.R.
663 Moradian, Fabrication new PES-based mixed matrix nanocomposite membranes using
664 polycaprolactone modified carbon nanotubes as the additive: Property changes and
665 morphological studies, Desalination, 277 (2011) 171-177.
666 [26] M. Irfan, H. Basri, M. Irfan, W. Lau, An acid functionalized MWCNT/PVP
667 nanocomposite as a new additive for fabrication of an ultrafiltration membrane with
668 improved anti-fouling resistance, Royal Society of Chemistry Advances, 5 (2015) 95421-
669 95432.
670 [27] M. Norouzi, M. Pakizeh, M. Namvar-Mahboub, The Effect of highly dispersed
671 oxidized multi-walled carbon nanotubes on the performance of PVDF/PVC ultrafiltration
672 membrane, Desalination and Water Treatment, 57 (2016) 24778-24787.
673 [28] J. Ma, X. Guo, Y. Ying, D. Liu, C. Zhong, Composite ultrafiltration membrane tailored
674 by MOF@GO with highly improved water purification performance, Chemical
675 Engineering Journal, 313 (2017) 890-898.
676 [29] J. Yin, G. Zhu, B. Deng, Multi-walled carbon nanotubes (MWNTs)/polysulfone (PSU)
677 mixed matrix hollow fiber membranes for enhanced water treatment, Journal of Membrane
678 Science, 437 (2013) 237-248.
679 [30] S. Majeed, D. Fierro, K. Buhr, J. Wind, B. Du, A. Boschetti-de-Fierro, V. Abetz, Multi-
680 walled carbon nanotubes (MWCNTs) mixed polyacrylonitrile (PAN) ultrafiltration

membranes, Journal of Membrane Science, 403-404 (2012) 101-109.
[31] A.K. Shukla, J. Alam, M. Alhoshan, L.A. Dass, M.R. Muthumareeswaran, Development of a nanocomposite ultrafiltration membrane based on polyphenylsulfone blended with graphene oxide, Scientific Reports, 7 (2017) 41976.
[32] M. Safarpour, A. Khataee, V. Vatanpour, Preparation of a Novel Polyvinylidene Fluoride (PVDF) Ultrafiltration Membrane Modified with Reduced Graphene Oxide/Titanium Dioxide (TiO2) Nanocomposite with Enhanced Hydrophilicity and Antifouling Properties, Industrial and Engineering Chemistry Research, 53 (2014) 13370-13382.
[33] W.S. Hummers, R.E. Offeman, Preparation of Graphitic Oxide, Journal of the American Chemical Society, 80 (1958) 1339-1339.
[34] Y. Jiang, W.N. Wang, D. Liu, Y. Nie, W. Li, J. Wu, F. Zhang, P. Biswas, J.D. Fortner, Engineered crumpled graphene oxide nanocomposite membrane assemblies for advanced water treatment processes, Environmental Science and Technology, 49 (2015) 6846-6854.
[35] Y. Jiang, D. Liu, M. Cho, S.S. Lee, F. Zhang, P. Biswas, J.D. Fortner, In Situ Photocatalytic Synthesis of Ag Nanoparticles (nAg) by Crumpled Graphene Oxide Composite Membranes for Filtration and Disinfection Applications, Environmental Science and Technology, 50 (2016) 2514-2521.
[36] Y. Jiang, R. Raliya, J.D. Fortner, P. Biswas, Graphene Oxides in Water: Correlating Morphology and Surface Chemistry with Aggregation Behavior, Environmental Science and Technology, 50 (2016) 6964-6973.
[37] M.-J. Han, Effect of propionic acid in the casting solution on the characteristics of phase inversion polysulfone membranes, Desalination, 121 (1999) 31-39.
[38] M. Dalwani, N.E. Benes, G. Bargeman, D. Stamatialis, M. Wessling, A method for characterizing membranes during nanofiltration at extreme pH, Journal of Membrane Science, 363 (2010) 188-194.

[39] W.S. Opong, A.L. Zydney, Diffusive and convective protein transport through asymmetric membranes, American Institute of Chemical Engineers Journal, 37 (1991) 1497-1510.
[40] J. Ren, Z. Li, F. Wong, A new method for the prediction of pore size distribution and MWCO of ultrafiltration membranes, Journal of Membrane Science, 279 (2006) 558-569.
[41] T. Szabó, O. Berkesi, P. Forgó, K. Josepovits, Y. Sanakis, D. Petridis, I. Dékány, Evolution of Surface Functional Groups in a Series of Progressively Oxidized Graphite Oxides, Chemistry of Materials, 18 (2006) 2740-2749.
[42] Y. Jiang, R. Raliya, P. Liao, P. Biswas, J.D. Fortner, Graphene oxides in water: assessing stability as a function of material and natural organic matter properties, Environmental Science: Nano, 4 (2017) 1484-1493.
[43] S.M. Aqeel, Z. Wang, L. Than, G. Sreenivasulu, X. Zeng, Poly(vinylidene fluoride)/poly(acrylonitrile) – based superior hydrophobic piezoelectric solid derived by aligned carbon nanotubes in electrospinning: fabrication, phase conversion and surface energy, Royal Society of Chemistry Advances, 5 (2015) 76383-76391.
[44] A.M. Rao, P. Eklund, S. Bandow, A. Thess, R.E. Smalley, Evidence for charge transfer in doped carbon nanotube bundles from Raman scattering, Nature, 388 (1997) 257.
[45] J. Wu, M. Lin, X. Cong, H. Liu, P. Tan, Raman spectroscopy of graphene-based materials and its applications in related devices, Chemical Society Reviews, 47 (2018) 1822-1873.
[46] A.C. Ferrari, J. Robertson, Interpretation of Raman spectra of disordered and amorphous carbon, Physical Review B, 61 (2000) 14095.
[47] A. Ganguly, S. Sharma, P. Papakonstantinou, J. Hamilton, Probing the Thermal Deoxygenation of Graphene Oxide Using High-Resolution In Situ X-ray-Based Spectroscopies, The Journal of Physical Chemistry C, 115 (2011) 17009-17019.
[48] H. Wang, A. Zhou, F. Peng, H. Yu, J. Yang, Mechanism study on adsorption of

733 acidified multiwalled carbon nanotubes to Pb(II), Journal of Colloid and Interface Science,
734 316 (2007) 277-283.
735 [49] M. Li, M. Boggs, T.P. Beebe, C.P. Huang, Oxidation of single-walled carbon
736 nanotubes in dilute aqueous solutions by ozone as affected by ultrasound, Carbon, 46 (2008)
737 466-475.
738 [50] P.C. Mishra, S. Mukherjee, S.K. Nayak, A. Panda, A brief review on viscosity of
739 nanofluids, International Nano Letters, 4 (2014) 109-120.
740 [51] E.V. Timofeeva, J.L. Routbort, D. Singh, Particle shape effects on thermophysical
741 properties of alumina nanofluids, Journal of Applied Physics, 106 (2009) 014304.
742 [52] D.K. Agarwal, A. Vaidyanathan, S.S. Kumar, Synthesis and characterization of
743 kerosene–alumina nanofluids, Applied Thermal Engineering, 60 (2013) 275-284.
744 [53] M. Sianipar, S.H. Kim, K. Khoiruddin, F. Iskandar, I.G. Wenten, Functionalized
745 carbon nanotube (CNT) membrane: progress and challenges, Royal Society of Chemistry
746 Advances, 7 (2017) 51175-51198.
747 [54] S. Ayyaru, Y. Ahn, Application of sulfonic acid group functionalized graphene oxide
748 to improve hydrophilicity, permeability, and antifouling of PVDF nanocomposite
749 ultrafiltration membranes, Journal of Membrane Science, 525 (2017) 210-219.
750 [55] N. Meng, R.C.E. Priestley, Y. Zhang, H. Wang, X. Zhang, The effect of reduction
751 degree of GO nanosheets on microstructure and performance of PVDF/GO hybrid
752 membranes, Journal of Membrane Science, 501 (2016) 169-178.
753 [56] J. Lee, H.-R. Chae, Y.J. Won, K. Lee, C.-H. Lee, H.H. Lee, I.-C. Kim, J.-m. Lee,
754 Graphene oxide nanoplatelets composite membrane with hydrophilic and antifouling
755 properties for wastewater treatment, Journal of Membrane Science, 448 (2013) 223-230.
756 [57] Z. Wang, H. Yu, J. Xia, F. Zhang, F. Li, Y. Xia, Y. Li, Novel GO-blended PVDF
757 ultrafiltration membranes, Desalination, 299 (2012) 50-54.
758 [58] E. Fontananova, V. Grosso, S.A. Aljlil, M.A. Bahattab, D. Vuono, F.P. Nicoletta, E.

759 Curcio, E. Drioli, G. Di Profio, Effect of functional groups on the properties of multiwalled
760 carbon nanotubes/polyvinylidenefluoride composite membranes, Journal of Membrane
761 Science, 541 (2017) 198-204.
762 [59] L.J. Zeman, A.L. Zydney, Microfiltration and ultrafiltration: principles and
763 applications, CRC Press, 1996.
764 [60] M. Sianipar, S.H. Kim, C. Min, L.D. Tijing, H.K. Shon, Potential and performance of
765 a polydopamine-coated multiwalled carbon nanotube/polysulfone nanocomposite
766 membrane for ultrafiltration application, Journal of Industrial and Engineering Chemistry,
767 34 (2016) 364-373.
768 [61] M. Elimelech, W.H. Chen, J.J. Waypa, Measuring the zeta (electrokinetic) potential of
769 reverse osmosis membranes by a streaming potential analyzer, Desalination, 95 (1994)
770 269-286.
771 [62] T.T.V. Tran, S.R. Kumar, S.J. Lue, Separation mechanisms of binary dye mixtures
772 using a PVDF ultrafiltration membrane: Donnan effect and intermolecular interaction,
773 Journal of Membrane Science, 575 (2019) 38-49.
774 [63] S. Mochizuki, A.L. Zydney, Dextran transport through asymmetric ultrafiltration
775 membranes: Comparison with hydrodynamic models, Journal of Membrane Science, 68
776 (1992) 21-41.
777 [64] Y. Akama, A. Tong, M. Ito, S. Tanaka, The study of the partitioning mechanism of
778 methyl orange in an aqueous two-phase system, Talanta, 48 (1999) 1133-1137.
779 [65] S.Y. Park, Y.J. Kim, S.Y. Kwak, Versatile surface charge-mediated anti-fouling UF/MF
780 membrane comprising charged hyperbranched polyglycerols (HPGs) and PVDF
781 membranes, Royal Society of Chemistry Advances, 6 (2016) 88959-88966.
782 [66] Shouren Ge, K. Kojio, A. Takahara, T. Kajiyama, Bovine serum albumin adsorption
783 onto immobilized organotrichlorosilane surface: Influence of the phase separation on
784 protein adsorption patterns, Journal of Biomaterials Science, Polymer Edition, 9 (1998)

131-150.

[67] G.M. Jordan, S. Yoshioka, T. Terao, The Aggregation of Bovine Serum Albumin in Solution and in the Solid State, Journal of Pharmacy and Pharmacology, 46 (1994) 182-185.